



Cite this: *Soft Matter*, 2015,
11, 7119

Tailor-made dimensions of diblock copolymer truncated micelles on a solid by UV irradiation[†]

Jiun-You Liou[‡] and Ya-Sen Sun*

We investigated the structural evolution of truncated micelles in ultrathin films of polystyrene-*block*-poly(2-vinylpyridine), PS-*b*-P2VP, of monolayer thickness on bare silicon substrates (SiO_x/Si) upon UV irradiation in air- (UVIA) and nitrogen-rich (UVIN) environments. The structural evolution of micelles upon UV irradiation was monitored using GISAXS measurements *in situ*, while the surface morphology was probed using atomic force microscopy *ex situ* and the chemical composition using X-ray photoelectron spectroscopy (XPS). This work provides clear evidence for the interpretation of the relationship between the structural evolution and photochemical reactions in PS-*b*-P2VP truncated micelles upon UVIA and UVIN. Under UVIA treatment, photolysis and cross-linking reactions coexisted within the micelles; photolysis occurred mainly at the top of the micelles, whereas cross-linking occurred preferentially at the bottom. The shape and size of UVIA-treated truncated micelles were controlled predominantly by oxidative photolysis reactions, which depended on the concentration gradient of free radicals and oxygen along the micelle height. Because of an interplay between photolysis and photo-crosslinking, the scattering length densities (SLD) of PS and P2VP remained constant. In contrast, UVIN treatments enhanced the contrast in SLD between the PS shell and the P2VP core as cross-linking dominated over photolysis in the presence of nitrogen. The enhancement of the SLD contrast was due to the various degrees of cross-linking under UVIN for the PS and P2VP blocks.

Received 8th July 2015,
Accepted 29th July 2015

DOI: 10.1039/c5sm01673h

www.rsc.org/softmatter

Introduction

UV irradiation (UVI), which induces photochemical reactions of materials, is an attractive technique for various applications such as the morphological design of block copolymers (BCP),^{1–3} surface coatings,⁴ micropatterns,^{5–9} pyrolyzed porous carbons,^{10–13} cellular engineering¹⁴ and shape-memory materials.¹⁵ For organic materials, the physical and chemical properties can be readily modified by UVI because the molecular constitution, chain configuration, composition, branching degree and molecular mass can be readily altered in photochemical reactions.

Department of Chemical and Materials Engineering, National Central University, Taoyuan 32001, Taiwan. E-mail: yssun@cc.ncu.edu.tw

† Electronic supplementary information (ESI) available: AFM topographic images and cross sections of micelles with UVIA at various time durations (Fig. S1 and S2), real-time experimental and simulated 2D GISAXS patterns of UVIA-treated micelles, which are displayed as animated figures (Fig. S3: movies 1 and 2), experimental and simulated intensity cross sections of GISAXS patterns (Fig. S4), contact angle values of a water droplet on the surface of UVIA-treated PS-*b*-P2VP micelles (Fig. S5), models and corresponding simulated 2D GISAXS patterns (Fig. S6), AFM topographic images of micelles upon UVIA of 60 min followed by immersion in organic solvents (Fig. S7) and solubility parameters of solvents, PS and P2VP (Table S1). See DOI: 10.1039/c5sm01673h

‡ Present address: Material and Chemical Research Laboratories, Industrial Technology Research Institute, Hsinchu, Taiwan.

The mechanism of UVI-induced photochemical reactions of polymer chains has been extensively investigated and reported. Two reaction routes – oxidative photodegradation (photolysis) and oxygen-free photo-stabilization (cross-linking) – are involved during UVI.^{7,9,16,17} Both routes depend on the concentration and mobility of free radicals created within an UV-irradiated polymer.^{7,9,16,17} The reaction route of photolysis, analogous to free-radical polymerization, has three major kinetic steps – initiation, propagation and termination. The first step is the formation of macro and hydrogen free radicals *via* UV-induced chain scission of carbon-hydrogen bonds along the backbone chains. In the presence of oxygen, the reaction of the macro free radicals with oxygen predominates in the second step to produce alkoxy polymer radicals. The peroxy radicals can further decompose into oxygen-containing species of small molecular mass *via* γ -scission reactions.¹⁷ In contrast, in the absence of oxygen, the propagation step is totally prohibited. The termination step, in which pairs of macro free radicals tend to recombine to form cross-linked polymeric chains, is thus dominant.

In contrast, UVI is able to induce cross-linking in polymers without exogenous cross-linking agents.^{1,5–17} This method offers a feasible procedure relative to other cross-linking methods. In particular, the advantages of UVI to trigger photochemical reactions include rapid photoreaction, small consumption of energy

and ease of process at ambient temperature and in solvent-free environments. In addition, UVI possesses minimal perturbation of polymers as the polymer itself acts as a cross-linking agent of zero length during the photochemical reaction. The chain cross-linking reaction is hence used to preserve the structures of polymers, which could further improve their thermal and chemical resistance.

UVI has been recently demonstrated to be able to stabilize effectively self-assembled nanodomains of BCP,^{2,3,10–13} or concurrently to degrade one minor block but to cross-link the other major block in BCP thin films.¹ The cross-linked nanodomains have great thermal stability and can thus serve as carbon precursors for subsequent fabrication of nanostructured carbons through carbonization at high temperature.^{10–13} An additional advantage of UVI stabilization is that cross-linked films have great solvent resistance.^{1–3} Fabricating multi-layered thin films with well-defined nanodomains is achieved upon UVI,^{2,3} or perforated nanoporous films can be achieved upon UVI followed by immersion in a solvent.¹ The mechanisms of UVI-induced reactions shaping or stabilizing the structural morphology and dimensions of self-assembled microdomains have yet to be clarified. Even scattering length densities of BCP thin films with UVI treatments have rarely been reported. In this work, we investigated systematically the structural evolution of micelles in PS-*b*-P2VP thin films of monolayer thickness under UVI in air (UVIA) and nitrogen (UVIN) by means of grazing incident X-ray scattering (GISAXS) *in situ* and atomic force microscopy (AFM) *ex situ*. By modeling simulations of the scattering data, we quantitatively acquired the shape, size, size distribution, lateral ordering and scattering-length density of UVIA- and UVIN-treated micelles on SiO_x/Si. To understand the photochemical reactions of UVIA- and UVIN-treated BCP thin films, we determined the chemical composition with X-ray photoelectron spectra (XPS) *ex situ*. The motivation of this research was to improve the understanding of relations between photochemical reactions and variations in the shape, dimensions and scattering length density of micelles.

Experimental section

Materials and sample preparation

PS-*b*-P2VP with a polydispersity index (PDI) of 1.13 and a molar mass of 118 500 g mol^{−1}, in which the molar masses of PS and P2VP are $M_n^{\text{PS}} = 48\,500 \text{ g mol}^{-1}$ and $M_n^{\text{P2VP}} = 70\,000 \text{ g mol}^{-1}$, respectively, was purchased from Polymer Source Inc. and used as received. All the organic solvents, including ethanol, acetic acid (HOAc), tetrahydrofuran (THF), acetone, toluene and *o*-xylene, were purchased from Aldrich without purification. According to procedures described elsewhere,¹⁸ we spin-coated a 0.3 wt% solution of PS-*b*-P2VP in *o*-xylene at 5000 rpm onto cleaned Si wafer substrates. The substrates were cleaned in piranha solutions (30% H₂O₂/98% H₂SO₄; 3/7, v/v) for 40 min, rinsed with deionized water 3 times, and subsequently dried under N₂ flow. In order to fully remove residual solvents from micellar films, the as-spun specimens were placed in a chamber with humidity less than 20% at 20–25 °C

(room temperature, RT). After complete drying, the micellar films were directly exposed to UV-irradiation (UV lamp: a germicidal lamp of G20T10 20 W light tube, SANKYO DENKI[®]). The irradiation intensity from the UV lamp was gauged using a UVX Radiometer (UVP, LLC) at a wavelength $\lambda = 254 \text{ nm}$ and the dosage was 2.4 mW cm^{−2} at a distance of 10 cm, which was the length used in all the experiments which included *in-situ* grazing-incident small-angle X-ray scattering (GISAXS), *ex situ* atomic force microscopy (AFM) and *ex situ* X-ray photoemission spectroscopy (XPS). The dosage investigated was between 1.44 J cm^{−2} and 77.76 J cm^{−2}, depending on the time intervals (from 10 min to 9 h) of UV irradiation.

Apparatus and characterization

AFM images were collected using an atomic force microscope (AFM, Seiko SPA400) in the tapping mode. The surface information was scanned and recorded with image sizes of 1 μm × 1 μm and 2 μm × 2 μm. Aluminum-coated silicon cantilevers were used with the force coefficient (k) of 7.4 N m^{−1}, and the resonant frequency (f) was 160 kHz (length: 150 μm, width: 26 μm, thickness: 300 μm). The images were gathered at a scan rate of 1 Hz and scanning pixels of 256 lines per frames. GISAXS measurements were implemented with a synchrotron X-ray radiation source at beamline BL23A1, National Synchrotron Radiation Research Center (NSRRC) at Hsinchu. The wavelength $\lambda = 1.24 \text{ \AA}$ was used, and GISAXS scattering patterns were collected using a two-dimensional detector (MarCCD 165 with a pixel array of 1024 × 1024 or PLATUS 1M-F). The scattering vectors in these GISAXS patterns were calibrated by a sample standard of silver behenate. To acquire scattering images with high signal-to-noise ratios, the angle of incidence of each X-ray beam was $\alpha_i = 0.2^\circ$, which is between the critical angle of the PS-*b*-P2VP film and the silicon substrates. The images were acquired with a data recording time of 10 s. Since GISAXS data reveal complicated scattering profiles or patterns as a result of multiple scattering events in terms of a combination of reflection and refraction effects, GISAXS modeling analyses can only be achieved using the distorted wave Born approximation (DWBA).^{19,20} In order to quantitatively obtain structural details, all the scattering 2D images and 1D profiles were simulated using the IsGISAXS software.²¹ The analysis of chemical components of micellar films was performed using a X-ray Photoelectron Spectroscopy (XPS) system (VG Scientific ESCALab 250) with a Mg K α radiation (max: 15 keV) and beam sizes of 120–650 μm.

Modeling of GISAXS data. To acquire quantitative details of micellar films with UVI on top of SiO_x/Si, both line cuts and whole 2D scattering patterns were calculated by the software IsGISAXS.²¹ To model the form factor, we used three types of micelle geometries, truncated core-shell sphere, truncated sphere and truncated cone (Fig. 1). The interference function of a hexagonal paracrystal of parameter D with Gaussian isotropic disorder σ_D/D was used to describe the spatial arrangement of UVI-treated micelles on the top of SiO_x/Si.¹⁸ Our previous work demonstrated that for as-spun PS-*b*-P2VP micelles each core-shell truncated sphere was looped in a circular mat comprised of mainly PS chains.¹⁸ To account for the observed intensity

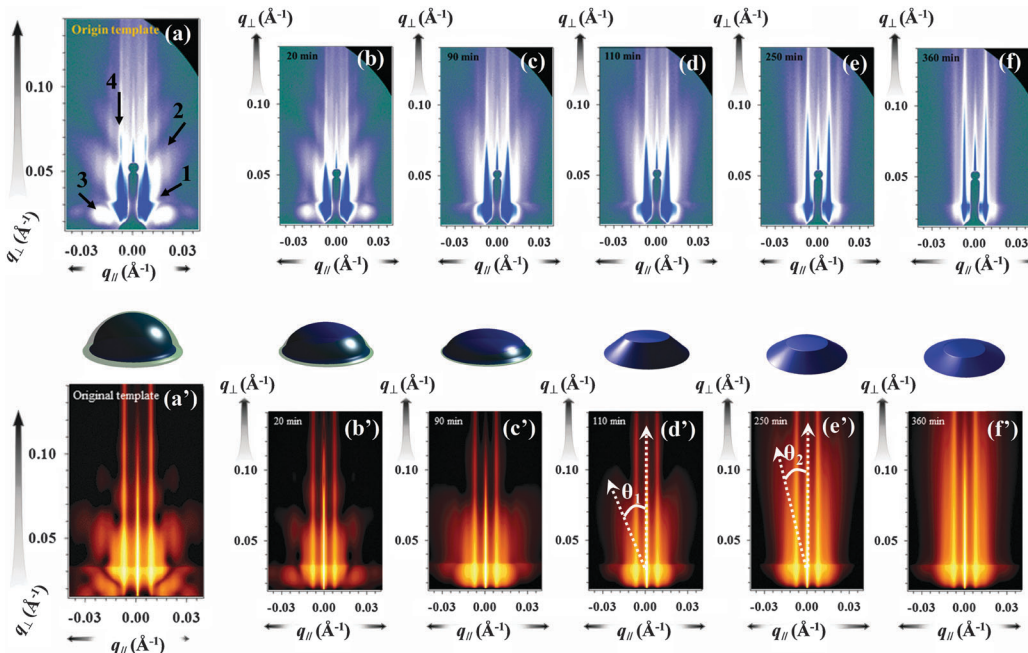


Fig. 1 Experimental and simulated GISAXS patterns of micellar films with UVIA of various time periods: (a) and (a') 0, (b) and (b') 20, (c) and (c') 90, (d) and (d') 110, (e) and (e') 250 and (f) and (f') 360 min. Three average micelle shapes are used, such as the core–shell truncated sphere, the truncated sphere and the truncated cone for model simulations. The intensity scale is logarithmic.

modulation along direction q_{\perp} , we introduced a parameter to describe a homogeneous layer of varied thickness L between a substrate and micellar objects in the simulations.¹⁸ As a result, through the modeling simulations, the structural parameters of the micelles with/without UVI can be calculated. For truncated core–shell sphere shape, the spatial ordering and structural parameters extracted from the fits include the nearest intermicelle distance (D), disorder parameter (σ_D/D), the average core radius ($\langle R \rangle$) and height ($\langle H \rangle$), size distribution of the core radius (σ_R), the normal and lateral thickness of the PS shell (dR and dH) and thickness (L) of the homogenous layer at the substrate interface. For truncated sphere shape, the simulated parameters were reduced as D , σ_D/D , $\langle R \rangle$, $\langle H \rangle$, and σ_R . For a truncated cone, an additional parameter, a base angle, was additionally considered for simulations of GISAXS data of severely UVI-treated micelles in air. For the modeling simulations, the SLDs of the pristine PS shell and P2VP core were respectively taken as $\rho_{PS} = 2 \times 10^{-6} \text{ \AA}^{-2}$ and $\rho_{P2VP} = 3 \times 10^{-6} \text{ \AA}^{-2}$. The SLD values varied with various dosages of UVIN but remained constant regardless of dosages of UVI. The different response of SLD to UVIN or UVIA treatments will be discussed in the following section.

Results and discussion

The real-space morphology of micelles with UVIA of various time periods was probed with AFM *ex situ*. As shown in Fig. S1 and S2 (ESI[†]), not only did UVIA cause decrease in the micellar thickness, but the micellar radius was also decreased by UVIA. The temporally resolved structural evolution of micelles with UVIA in reciprocal space was investigated with GISAXS measurements

in situ. Fig. 1 shows selected experimental GISAXS 2D patterns and the corresponding simulated patterns of these UVIA-treated films. The real-time experimental and simulated 2D GISAXS patterns are stacked frame by frame and are displayed as animated figures (see Fig. S3, ESI[†]). Before UVIA, the as spun PS-*b*-P2VP micelles reveal four prominent features: an intensity modulation present at the bottom of the calabash-shaped scattering (label 1), inclined diffuse-scattering rods with respect to the substrate normal (label 2), scattering spots along the q_{\parallel} direction (label 3) and narrow Bragg diffraction streaks (label 4) (Fig. 1a). The inclined diffuse-scattering rods interfered coherently with the Bragg diffraction streaks to cause elongated bands. These scattering features were well reproduced with modeling simulations with IsGISAXS according to the model of core–shell truncated spheres with a paracrystalline spatial order (Fig. 1a'). The first three features are associated with the form factor of truncated spheres with a core–shell structure whereas the last one corresponds to the structure factor of truncated spheres with a short-range spatial order.¹⁸ According to the model, the structural parameters were quantitatively known for pristine PS-*b*-P2VP micelles; the P2VP cores have an average height $\langle H \rangle$ of 23.7 nm and a radius $\langle R \rangle$ of 27.2 nm whereas the PS shells in the dry state had anisotropic thickness, in which shell thickness dR normal to the substrate was 2.9 nm and shell thickness dH along the substrate was 1.2 nm. The truncation of nanospheres is ascribed to wetting of micelles on the surface of a solid substrate. Such a wetting behavior is analogous to the wetting of liquid droplets on the surface.²² When micelles adhered to a solid flat surface, they deformed through truncation along the substrate normal to appear in a truncated shape.¹⁸

Upon UVIA, variations in the scattering features were present in the GISAXS patterns (see Fig. S3a (ESI[†]) and Fig. 1b–f).

Firstly, the intensity modulation with label 2 gradually weakened with increasing duration of Uvia during the first 90 min and completely vanished later. In addition, the scattering spots moved towards larger q_{\parallel} and q_{\perp} . The shift of the scattering spots to small values of q_{\parallel} and q_{\perp} with varied durations of Uvia was accompanied by a decreased scattering intensity (see Fig. 1b–c). At the final stage of Uvia (>110 min), the scattering spots completely vanished (Fig. 1d–f). Furthermore, the angle between the inclined scattering rods and the q_{\perp} direction decreased with increasing UV dosage. In contrast, the position of the Bragg streaks remained unchanged during the entire process of Uvia. This result indicates that Uvia produced only a structural change of micelles but did not influence their spatial order.

Simulations with IsGISAXS were performed to analyze quantitatively the structural details of Uvia-treated micelles. Considering that the micelle spatial order was not influenced by Uvia, the same paracrystalline order model was used to simulate the structure-factor diffraction of Uvia-treated micelles. As Uvia altered only the micellar shape and dimensions, the model of truncated spheres with a core–shell structure was inapplicable to simulate the GISAXS data of Uvia-treated micelles. As shown in Fig. S3b (ESI†) and Fig. 1c'–f', the best fits were obtained with shell-free truncated spheres for mildly Uvia-treated micelles (Fig. 1c') and with a shell-free truncated cone for severely Uvia-treated ones (Fig. 1d'–f').

Both the simulated 2D GISAXS patterns (Fig. 1a'–f') and simulated 1D in-plane and out-of-plane scan profiles (Fig. S4, ESI†) show a perfect consistency with the experimental GISAXS data. The SLD values of Uvia-treated PS and P2VP chains used in fitting were notably the same as those of their pristine state. The P2VP core, PS shell and layer thicknesses of the truncated micelles extracted from the simulated patterns and profiles are plotted as functions of UV exposure duration in Fig. 2. For the PS shell and underlying homogenous layer, the thicknesses – dR , dH and L – were rapidly degraded with Uvia. Until 60 min, the PS shell was totally degraded with Uvia whereas the underlying layer was completely degraded at 100 min of Uvia (see Fig. 2a). For the P2VP core, two regimes are distinguished in the evolution of $\langle H \rangle$ upon increasing UV exposure duration, with a change in behavior at 100–120 min (see Fig. 2b). $\langle H \rangle$ decreased rapidly in the first region; the decrease slowed down over time in the second regime. In contrast, the decrease in $\langle R \rangle$ with time was much slower than $\langle H \rangle$ in the first regime. In the second regime, $\langle R \rangle$ decreased in size at the same rate as $\langle H \rangle$. According to the dimensional evolution of PS-*b*-P2VP micelles with the duration of Uvia, we identified two regimes (briefly denoted as regimes I and II), in which anisotropic and isotropic degradation controlled the dimensional change in Uvia-treated P2VP cores.

To help clarify the roles of surface oxidation and degradation of PS and P2VP chains during Uvia, we probed the evolution of the surface chemistry of PS-*b*-P2VP micelles before and after Uvia with XPS (Fig. 3). Fig. 3a shows XPS carbon 1s (C 1s) spectra for micelles before and after Uvia; XPS C 1s spectra of the pristine micellar film reveal only a line at 285 eV and a satellite line at 291.5 eV. The former line results from the superimposition of two contributions – aromatic carbons and hydrocarbons (at 285 eV)

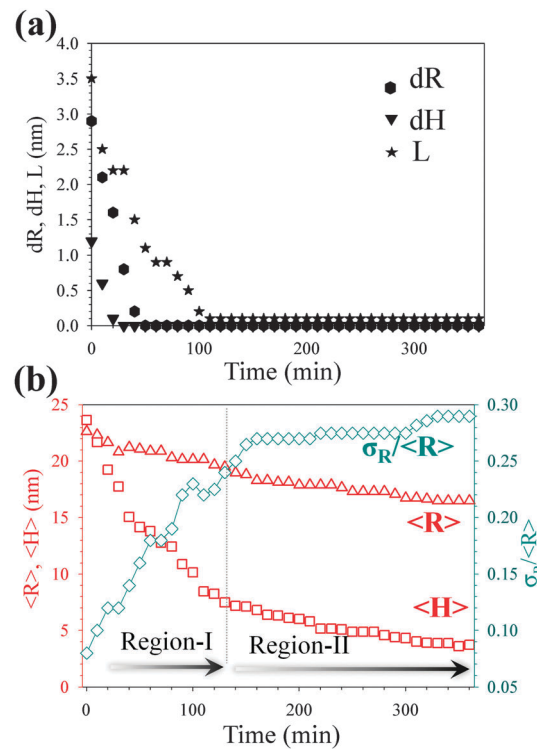


Fig. 2 (a) Dependence of Uvia time on thickness (dR : filled hexagons; dH : filled triangles down) of PS shells and thickness (L : filled stars) of the homogeneous layer at the substrate interface. (b) Plots show the variation of the core size (radius $\langle R \rangle$: open triangles; height $\langle H \rangle$: open squares), and size distribution ($\sigma_R/\langle R \rangle$ open diamonds) with various times of Uvia.

and carbons bonded to nitrogen (at 286.2 eV), whereas the latter line is attributed to the shake-off line of polystyrene.²³ Upon Uvia for 30 min, the two lines at 285 and 291.5 eV showed decreased intensities but the line at 286.2 eV showed an enhanced intensity.^{24–26} The three new lines begin to merge at large binding energies, and become more evident with greater durations (160 and 320 min) of Uvia. The three lines centered at 285.4, 286.5 and 288.1 eV are attributed to those groups involving C–OH, C–O–C and C=O bonds, respectively. This result indicates that Uvia caused oxidative reactions of the aromatic rings and aliphatic carbons with oxygen to yield oxygen-containing carbon groups.

To make a quantitative analysis of XPS lines, we decomposed the C 1s spectra (software Origin 8.5). Since Uvia caused the loss of carbon and nitrogen species, the pristine state was regarded as a reference to calculate residual yields of C and N first for the Uvia-treated micellar films. The relative compositions of the carbon species (C–C/C=C, C–H, C–OH, C–O–C and C=O) were calculated based on the residual yields and plotted to show the dependence of composition variation on duration of Uvia. As Fig. 3b shows, Uvia caused the oxidation of polymer chains, evident from a rapid decrease in the content of the C–C/C=C component and from the growth of oxygen-containing species. As the inset shows, the content of C–OH, one oxygen-containing product, increased rapidly after brief Uvia. In comparison with the immediately decreased composition of

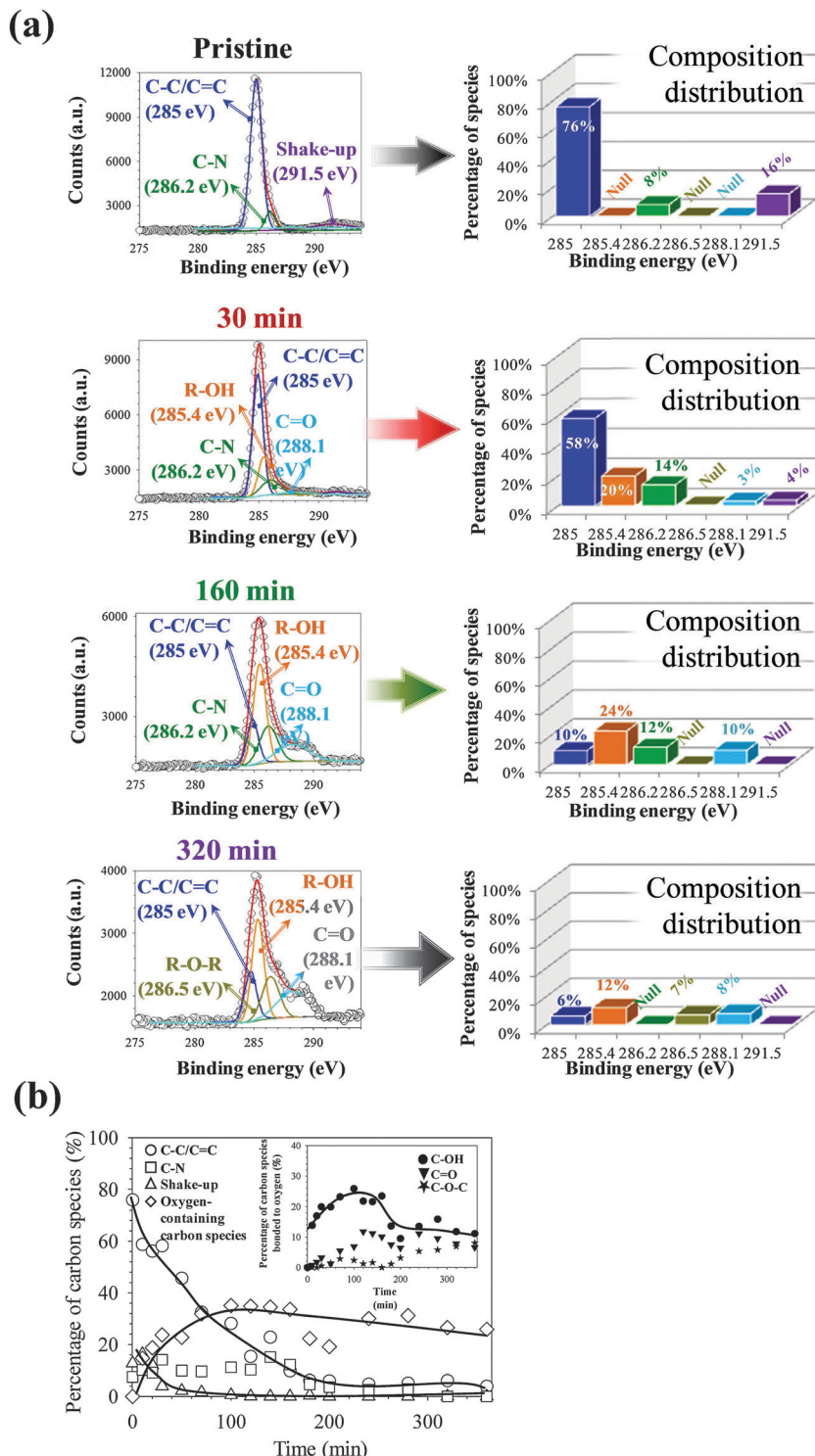


Fig. 3 (a) XPS C 1s spectra of PS-*b*-P2VP micellar films with UVIA of varied durations. Decomposition of the XPS peaks was done using the software Origin 8.5 for revealing the distributions of composition of carbon species. The fitted peaks are C-C/C=C at 285 eV (blue), C-OH at 285.4 eV (orange), C-N at 286.2 eV (green), C=O-C at 286.5 eV (brown), C=O at 288.1 eV (cyan) and a shake-up peak at 291.5 eV (purple). (b) Percentage of oxygen-free and oxygen-containing carbon groups as a function of the duration of UVIA for PS-*b*-P2VP micellar films. The inset in the upper right represents the time dependence of percentage of C-OH, C=O-C and C=O for the oxygen-containing carbon groups. The solid lines are plotted to serve as a visual guide.

the C-C/C-H and aromatic rings, at early stages of UVIA the growth curve of C-OH was more rapid than that of C=O-C and C=O through the breaking of C=C groups and destruction of

C-H groups on implanting oxygen radicals. As a result, the content of C-OH was a major proportion and C=O-C and C=O were present in minor proportions. Upon prolonged UVIA, the

C=O content reached a plateau regime while the C–O–C content further grew at the expense of partial C–OH species. This result indicates that C–OH was an intermediate product of C–O–C.

To understand the oxidation and degradation of the P2VP core, we focused on nitrogen 1s (N 1s) XPS results. Fig. 4a shows N 1s XPS spectra and corresponding fits for micellar films with UVIA. The calculated composition of each component

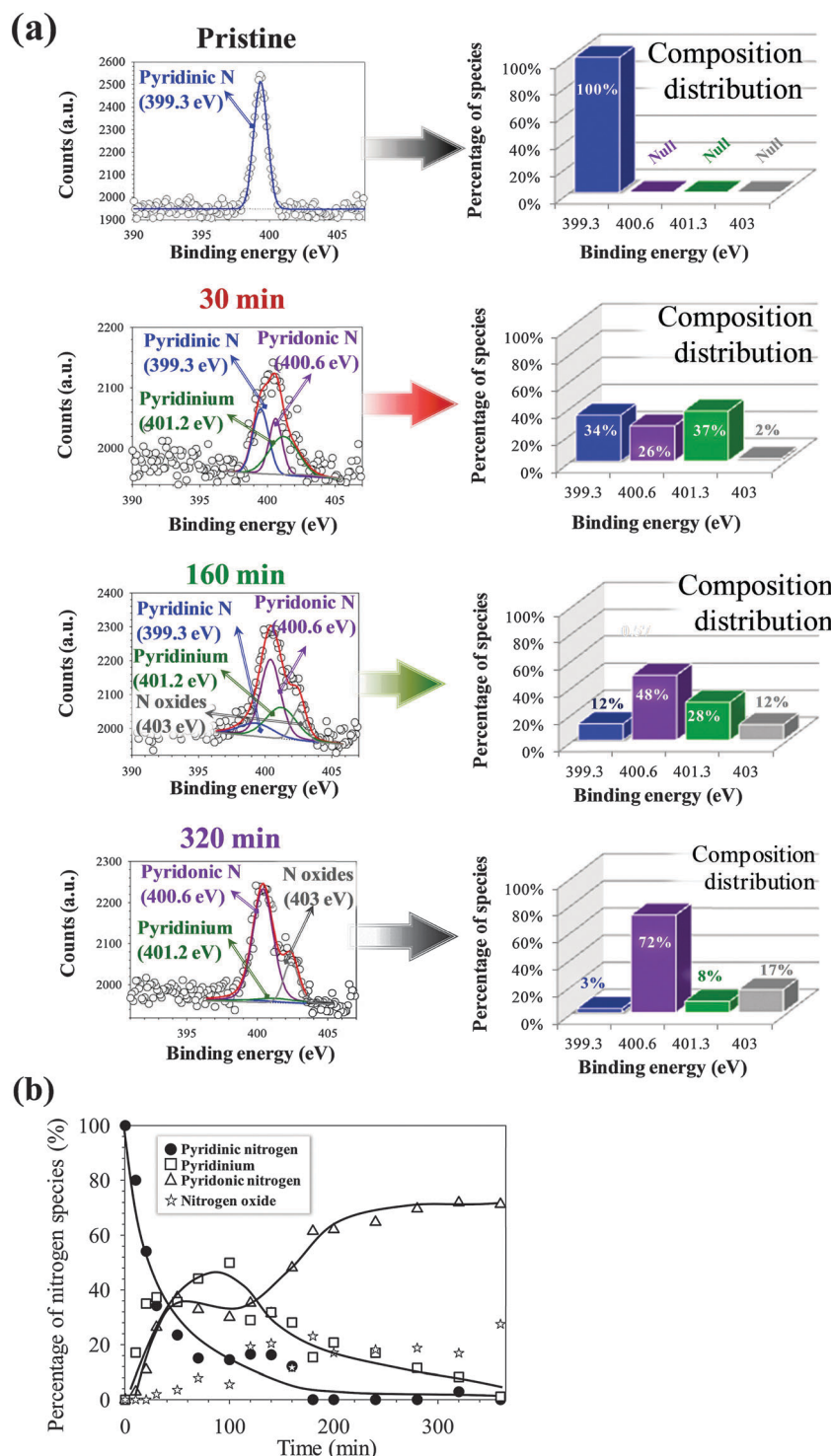


Fig. 4 (a) XPS N 1s spectra of PS-*b*-P2VP micellar films with UVIA of varied durations. Decomposition of the XPS peaks was done using the software Origin 8.5 for revealing the distributions of composition of carbon species. The fitted peaks are pyridinic nitrogen at 399.3 eV (blue), pyridonic nitrogen at 400.6 (purple), pyridinium at 401.2 eV (green) and nitrogen oxide at 403 eV (gray). (b) Percentage of nitrogen-containing species as a function of the duration of UVIA for PS-*b*-P2VP micellar films. The solid lines are plotted to serve as a visual guide.

is also displayed in Fig. 4a for a quantitative comparison. Before UVIA, the pyridinic nitrogen of P2VP chains reveals a line at 399.3 eV.^{27,28} After UVIA, the pyridine ring of the P2VP block was oxidized and protonated to form three nitrogen-containing groups such as pyridonic nitrogen (400.6 eV), pyridinium (401.2 eV) and nitrogen oxide (403 eV).^{27,28} A comparison of N 1s XPS spectra of UVIA-treated micellar films indicates that the three nitrogen-containing groups exhibit varied dominant content at various durations of UVIA, depending on the extent of oxidative reactions of pyridinic rings with molecular oxygen. Quantitative analysis of elemental composition indicates that the sample treated with UVIA for 30 min had a greater content of pyridonic nitrogen, slightly less pyridinium and much less nitrogen oxide. Upon UVIA for 160 and 320 min, pyridonic nitrogen and nitrogen oxide contents are greater than that of pyridinium. This result indicates that both pyridonic nitrogen and nitrogen oxide predominate in the formation of nitrogen-containing species at the final stage of UVIA.

Fig. 4b shows the changes of composition of nitrogen-containing groups with the duration of UVIA: at early stages of UVIA, the content of both pyridonic nitrogen and pyridinium exponentially increased with increasing time. This result indicates that the early stage of UVIA caused oxidative reactions of pyridine nitrogen with oxygen to form pyridonic nitrogen and H-transfer reactions from CH₂ groups along the vinyl backbone to the N atom of the pyridine ring to yield pyridinium.²⁹ After rapid – exponential – growth, pyridonic nitrogen remained stable for a short period and then grew at the expense of pyridine nitrogen through oxidative reactions. A two-step growth was thus observed for pyridonic nitrogen. In contrast, pyridinium was unstable, and quickly transformed into nitrogen oxide when the duration of

UVIA reached about 100 min. As the oxidative reaction between pyridine rings and pyridinium was competitive, the oxidation of pyridinium thus interfered with that of the pyridine ring. Such a competition led to a two-step growth of pyridonic nitrogen. Once the growth of nitrogen oxide slowed down, both pyridonic nitrogen and nitrogen oxide were dominant species at the final stage of UVIA.

After performing UVIA for various periods of time, the surface of the PS-*b*-P2VP micelles become more and more hydrophilic with time, evidenced by the reduced contact angle values of a water droplet from 97.6° (with 10 min UVIA) to 33.8° (with 540 min UVIA) (see Fig. S5, ESI†). This result indicates that the altered surface property of the UVIA-treated PS-*b*-P2VP micelles depends on the various extents of oxidation of the PS and P2VP blocks.

The structural details of micelles with UVIN were investigated with GISAXS measurements. Fig. 5 shows the experimental GISAXS 2D patterns of these films with UVIN for 3, 4, 6 and 9 h and their corresponding simulated patterns. As shown in Fig. 5a–d, the four features for ordered arrays of truncated spheres with a core–shell structure are still observable, indicating that UVIN did not change the order or even the shape, but the UVIN-treated films show two distinct scattering features, respectively near the Yoneda peak and along the inclined diffusion-scattering rods (marked with arrows).

The 2D GISAXS results were simulated with IsGISAXS again. The best simulation results were obtained with IsGISAXS based on the model of core–shell truncated spheres (see Fig. 5e–h). The observed intensity features were generally well reproduced in particular when the scattering length density (SLD) of the PS shell was greater than that of the P2VP core (see Fig. 5e–h and Fig. S6a, ESI†). We tried

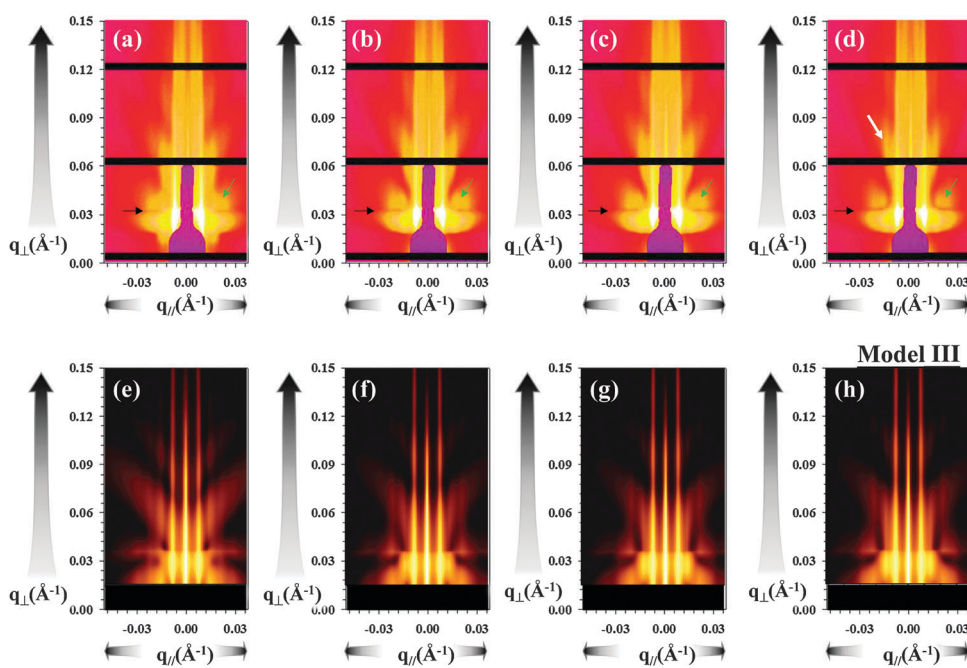


Fig. 5 2D GISAXS experimental (a–d) and simulation (e–h) patterns of UVIN-treated films of PS-*b*-P2VP for 3 (a and e), 4 (b and f), 6 (c and g), and 9 h (d and h). The intensity scale is logarithmic.

another model, homogeneous truncated spheres without core-shell electron-density contrast (see Fig. S6b, ESI†), but that model was unsuccessful to reproduce the distinct scattering features. The parameters of the simulated GISAXS patterns are shown in Table 1. For as spun micelles, the SLD of PS was slightly less than that of P2VP before UVIN. After UVIN, SLD increased for both PS and P2VP; the SLD of PS increased more rapidly than that of P2VP (Table 1). As a result, the contrast in electron density between PS and P2VP was enhanced with UVIN. The enhanced contrast

Table 1 Structural parameters used for the simulated GISAXS patterns of UVIN-treated micelles

Simulated parameters	UVIN periods				
	3 h	4 h	6 h	9 h	
SLD (\AA^{-2})	$\delta_{\text{Core}} \times 10^6$	3.0	3.6	4.2	3.7
	$\delta_{\text{shell}} \times 10^6$	5.7	6.8	7.0	7.0
Bottom layer, nm		1.1	1.0	1.0	1.0
$\langle R \rangle$, nm		34	29	27	26
$\langle H \rangle$, nm		19.4	17.1	17	16.7
Radius distribution, nm		5.5	3.5	3.3	2.6
Shell structures	dR , nm	7.5	6.9	6.1	6.0
	dH , nm	2.5	2.5	2.5	2.5

produced pronounced form-factor scattering of a core–shell structure. In addition to the scattering contrast between cores and shells, the micelles shrank significantly after UVIN; the extent of dimensional shrinkage depended on UV irradiation dosage. Because of the nitrogen-filled environment, it is likely that UVIN led to crosslinking reactions of polymer chains. The increment of the scattering-length density contrast between P2VP cores and PS shells and dimensional shrinkage is thus attributed only to an increased degree of cross-linking of polymer chains imparted by UVIN.

Fig. 6 shows C 1s XPS of UVIN-treated micellar films. Relative to UVIA-treated micelles, the UVIN-treated micelles have greater content of the C=C/C=C component at 285 eV, less C–N (at 286.2 eV) and much less C–OH (at 285.6 eV) components, and trace C=O component at 288.1 eV. This result indicates that the oxidative reaction of carbons was significantly decreased under UVIN. Fig. 7 shows XPS N 1s of the UVIN-treated micellar films, in which the pyridinic-N line at 399.3 eV decreased in intensity, while the 400.3 and 401.2 eV lines showed an opposite trend when UVIN was imposed on PS-*b*-P2VP micellar films. The latter two lines correspond to pyrrolic nitrogen and pyridinium, respectively.²⁷ These results

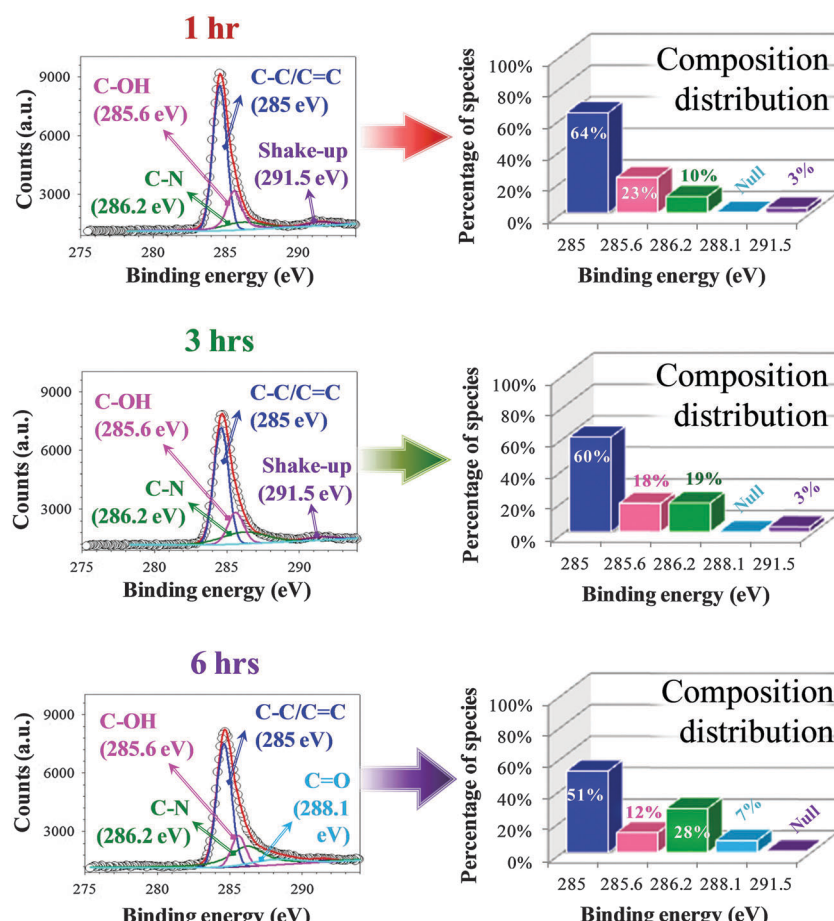


Fig. 6 XPS C 1s spectra of PS-*b*-P2VP micellar films with UVIN of varied durations. Decomposition of the XPS peaks was done using the software Origin 8.5 for revealing the distributions of composition of carbon species. The fitted peaks are C–C/C=C at 285 eV (blue), C–OH at 285.6 eV (pink), C–N at 286.2 eV (green), C=O at 288.1 eV (cyan) and a shake-up peak at 291.5 eV (purple).

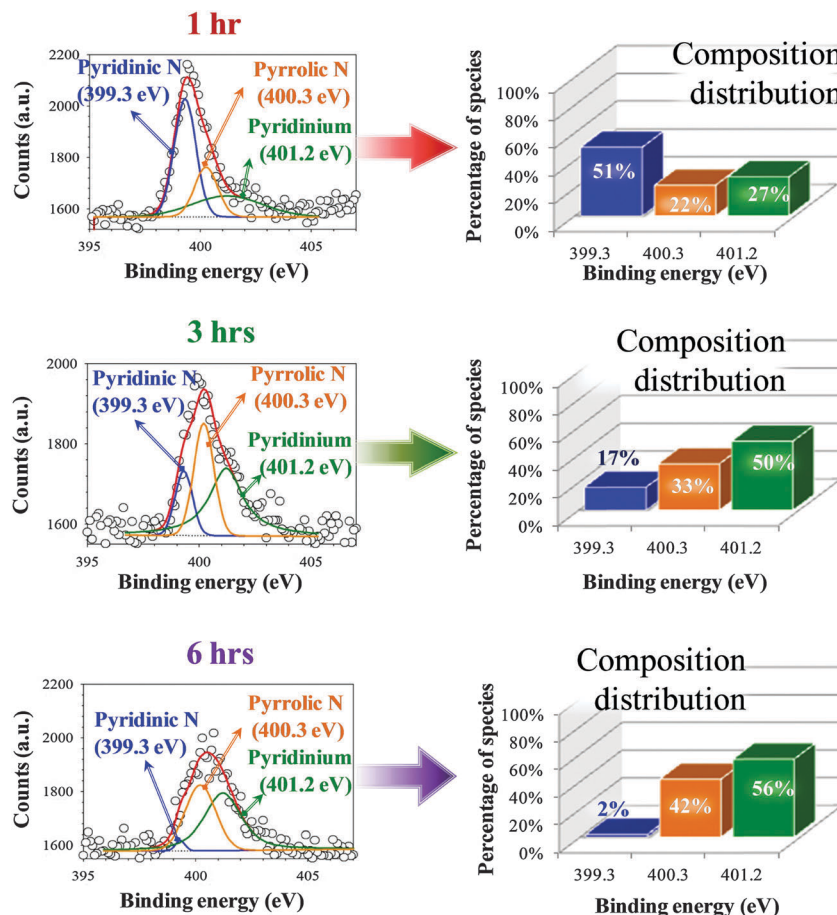


Fig. 7 XPS N 1s spectra of PS-*b*-P2VP micellar films with UVIN of varied durations. Decomposition of the XPS peak was done using the software Origin 8.5 for revealing the distributions of carbon species. The fitted peaks are pyridinic nitrogen at 399.3 eV (blue), pyrrolic nitrogen at 400.3 eV (orange) and pyridinium at 401.2 eV (green).

reveal that, under UVIN, pyrrolic nitrogen and pyridinium steadily yielded and grew at the expense of pyridinic nitrogen. In contrast, oxygen-containing nitrogen species were totally absent for the UVIN-treated micelles, indicating that the oxidation reaction was completely prohibited for the P2VP block. The pyrrolic nitrogen and pyridinium were thus stable once formed.

On the basis of our modeling simulations of the GISAXS scattering patterns and quantitative analysis of the XPS spectra, we propose a series of scenarios to describe the shape, size, size distribution and assembled arrays of micelles at varied dosages of exposure to UVIA and UVIN. Before either UVIA or UVIN, the as spun micelles exhibit shell-truncated spheres with a core shell structure. The PS shells in a dry state have an anisotropic thickness; shell thickness dH normal to the substrate is much less than shell thickness dR along the substrate. Upon UVIA, the PS shell and homogenous layer degraded rapidly and were totally removed after UVIA for 60 min. The shape of the micelles changed from core-shell truncated spheres to shell-free truncated spheres. For the P2VP core, degradation was anisotropic at an early stage of UVIA, at which the degradation of the core height was more rapid than that of the core radius. Upon prolonged UVIA (> 110 min), the degradation became isotropic: both lateral core radius and height degraded at the same rate.

As a result, the micellar shape altered from a truncated sphere to a truncated cone. We ascribe the anisotropic degradation to competitive reactions between photolysis and photo-crosslinking. The kinetics of photolysis depend on the rate of adsorption of oxygen on the surface of micelles, the oxygen permeability³⁰ in micelles, the rate of formation of free radicals and the rate of the oxidative reaction.¹⁷ Quantitative analysis of C and N 1s XPS spectra indicates that UVIA-induced photolysis was controlled by oxidative reactions of high order. The rate of the high-order oxidative reaction thus depended on the concentrations of both oxygen and free radicals within the UV-irradiated micelles. The oxygen concentration was controlled mainly by oxygen permeability within micelles whereas the concentration of free radicals was controlled by UV dosage. At early stages of UVIA, polymeric degradation occurred *via* chain-scission reactions mainly along the vinyl polymeric backbone to form free radicals first. As the top surface and inner bottom of the micelles experienced disparate UV dosages because of different distances to UV light and the attenuation of the UV light by the top surface, the concentration of free radicals is thus greatest at the top of the micelles and least at the bottom, producing a concentration gradient of free radicals along the normal direction (see Fig. 8).

Oxygen was adsorbed onto the surface of micelles from air and diffused through the micelles, traveling along the concentration gradient (Fig. 8). In the presence of oxygen, subsequent oxidative reactions of the free radicals became a dominant path when cross-linking formed by a recombination of macro free radicals was sluggish. Once oxygen was attached to the free radicals, cross-linking was totally prohibited; the chain-scission reaction thus propagated to form volatile oxygen-containing oligomers. As the thickness of the PS shell was less along the normal direction than along the lateral direction, the concentration of oxygen was expected to be greater within the top of the P2VP core. Large concentrations of both oxygen and free radicals at the top of the core account for the rapid two-step degradation of the P2VP core along the normal direction.

In contrast, when oxygen diffusion was retarded by a barrier, the free radicals tended to recombine. As a result, photo-crosslinking became dominant over photolysis, which in turn further inhibited oxygen diffusion. The reason is that the free volume of micelles became significantly decreased through crosslinking, impeding oxygen diffusion. As the PS shell was thick along the core radius and acted as a barrier for oxygen diffusion, cross-linking was dominant over photolysis for the core radius under UVIA, leading to the slow one-step degradation of the core radius.

We next discuss how UVIN enhanced the electron contrast between the PS shell and the P2VP core. UVI induced formation of free hydrogen and macromolecular radicals through chain-scission reactions along the polymeric backbone. In an environment of nitrogen gas, the oxidative reaction of the free radicals was significantly decreased (see Fig. 8); the recombination reaction of the free radicals thus predominated. For UVIN-treated PS, in addition to chain cross-linking between macro free radicals, the major side product was hydrogen, which easily evaporated from the linked polymer matrix to the air. Cross-linking also decreased the free volume, as evident from

the UVIN-induced dimensional shrinkage. Both factors led to an increased mass density of the PS shell. In contrast, for UVIN-treated P2VP, UVIN induced formation of pyrrolic species *via* the loss of carbons from pyridine rings and the formation of free hydrogen radicals. The free hydrogen radicals exhibited a strong tendency to get adsorbed on the nitrogen of pyridine rings *via* H-transfer reaction. Although cross-linking also caused a volume shrinkage of the P2VP core, the loss of carbons from pyridine rings created voids within the P2VP core. Through the interplay between the shrinkage volume of cross-linked P2VP cores and voids formed within the P2VP cores, the scattering length density of UVIN-treated P2VP increased only slightly. This explanation also accounts for the unchanged SLD values for UVIA-treated micelles. Our previous work on X-ray reflectivity of structural details of PS grafted chains treated with UV and ozone indicated that both oxidation and degradation decreased SLD.³¹ The reason is that oxygen-containing groups produced through the oxidative photo-degradation reactions were volatile and evaporated easily from the polymeric matrix to the air, leading to the formation of voids within the polymeric matrix. For UVIA-treated micelles, such oxidative photo-degradation reactions occurred rapidly at the top surface of the micelles because in that region the concentrations of both oxygen and free radicals were greatest (see Fig. 8). Cross-linking, accounting for an increased SLD, concurrently occurred, however, and predominated at the bottom of the micelles. To identify whether photolysis existed at the top of micelles and photo-crosslinking predominated at the bottom, we conducted a simple experiment of removing micelles through sonication of the film-covered substrates in organic solvents after the films were subjected to protracted UVIA (60 min). If chains were cross-linked under UVIA, the removal of BCP micelles from SiO_x/Si would be unlikely, but, if chains become oxidized to form oxygen-containing species, these species would dissolve easily in solvents. Fig. S7 (ESI[†]) shows that, after 60 min of UVIA followed by sonication in solvents, only the top of the micelles was oxidized by UVIA and could be removed using polar organic solvents, such as acetone, acetic acid and THF, with solubility in the range 19 and 22 MPa^{1/2} (see Table S1, ESI[†]). In contrast, the bottom of the micelles still adhered to the SiO_x/Si . As a result, only the height of the UVIA-treated micelles decreased whereas the micellar diameter remained constant. This result indicates that photolysis and photo-crosslinking occurred concurrently within the micelles treated with UVIA. We thus conclude that the interplay between photolysis and photo-crosslinking does not alter the SLD values of the UVIA-treated micelles.

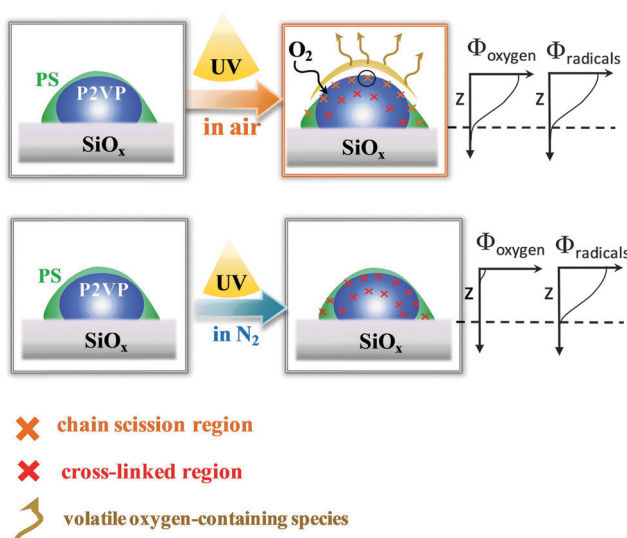


Fig. 8 Schematic illustration of the core–shell truncated sphere with UVIA and UVIN treatments. Φ denotes the concentration gradient.

Conclusion

In summary, we demonstrate a simple method to produce self-assembled PS-*b*-P2VP truncated micelles with tunable dimensions and shape tailored by UVIA and UVIN. When spin-coated PS-*b*-P2VP truncated micelles were treated with UVIA for varied durations, the truncated micelles degraded in the presence of

oxygen. Quantitative analysis through model simulations of the X-ray scattering patterns revealed that the oxidative photo-degradation of the PS shell and the underlying layer was much more rapid than for the P2VP core during UVIA. The P2VP core during UVIA involved two-stage kinetics involving the coexistence of photolysis and photo-crosslinking. Degradation of the P2VP core was anisotropic at an early stage of UVIA, at which the rate of degradation of the core height was more rapid than that of the core radius. Upon prolonged UVIA, the degradation became isotropic: both lateral radius and height of the P2VP core degraded at the same rate. As a result, the micellar shape altered from a truncated sphere to a truncated cone. A comparison between GISAXS and XPS analysis indicated that the difference in photo-oxidized degradation kinetics between radius and height was due to the concentration gradient of free radicals along the height direction. The reason is that the amount of radicals produced through chain scission of polymeric chains with UVIA depended on the distance between the lamp and the exposed area. In contrast, upon UVIN, chain cross-linking reactions predominated over chain-scission reactions so that the micellar nanostructures became stabilized to possess effective solvent and thermal resistance.

Acknowledgements

Ministry of Science and Technology (MOST) provided support (NSC-100-2628-E-008-007-MY3 and MOST 103-2221-E-008-084-MY3).

References

- P. Zavala-Rivera, K. Channon, V. Nguyen, E. Sivaniah, D. Kabra, R. H. Friend, S. K. Nataraj, S. A. Al-Muhtaseb, A. Hexemer, M. E. Calvo and H. Miguez, *Nat. Mater.*, 2010, **11**, 53–57.
- H. Jung, D. Hwang, E. Kim, B.-J. Kim, W. B. Lee, J. E. Poelma, J. Kim, C. J. Hawker, J. Huh, D. Y. Ryu and J. Bang, *ACS Nano*, 2011, **5**, 6164–6173.
- E. Kim, C. Shin, H. Ahn, D. Y. Ryu, J. Bang, C. J. Hawker and T. P. Russell, *Soft Matter*, 2008, **4**, 475–479.
- P. M. Imbesi, N. V. Gohad, M. J. Eller, B. Orihuela, D. Rittschof, E. A. Schweikert, A. S. Mount and K. L. Wooley, *ACS Nano*, 2012, **6**, 1503–1512.
- T. Tischer, C. Rodriguez-Emmenegger, V. Trouillet, A. Welle, V. Schueler, J. O. Mueller, A. S. Goldmann, E. Brynda and C. Barner-Kowollik, *Adv. Mater.*, 2014, **26**, 4087–4092.
- L. Li, Y. Zhong, J. Li, C. Chen, A. Zhang, J. Xu and Z. Ma, *J. Mater. Chem.*, 2009, **19**, 7222–7227.
- M. Yan and B. Harnish, *Adv. Mater.*, 2003, **15**, 244–248.
- S. Chada and M. Yan, *Soft Matter*, 2008, **4**, 2164–2167.
- E. J. Park, G. T. Carroll, N. J. Turro and J. T. Koberstein, *Soft Matter*, 2009, **5**, 36–50.
- Y. Wang, J. Q. Kiu, S. Christiansen, D. H. Kim, U. Goesele and M. Steinhart, *Nano Lett.*, 2008, **8**, 3993–3997.
- D. A. Rider, L. Kun, J.-C. Eloi, L. Vanderark, L. Yang, J.-Y. Wang, D. Groza, Z.-H. Lu, T. P. Russell and I. Manners, *ACS Nano*, 2008, **2**, 263–270.
- Y. H. Jang, X. Xin, M. Byun, Y. J. Jang, Z. Lin and D. H. Kim, *Nano Lett.*, 2012, **12**, 479–485.
- Z. Li, D. Wu, Y. Liang, F. Xu and R. Fu, *Nanoscale*, 2013, **5**, 10824–10828.
- L. Li, C. Chen, J. Li, A. Zhang, X. Liu, B. Xu, S. Gao, G. Jin and Z. Ma, *J. Mater. Chem.*, 2009, **19**, 2789–2796.
- S.-K. Ahn, P. Deshmukh, M. Gopinadhan, C.-O. Osuji and R.-M. Kasi, *ACS Nano*, 2011, **5**, 3085–3095.
- B. Harnish, J. T. Robinson, Z. Pei, O. Ramström and M. Yan, *Chem. Mater.*, 2005, **17**, 4092–4096.
- J. F. Raberk and B. Rånby, *J. Polym. Sci., Polym. Chem. Ed.*, 1974, **12**, 273–294.
- J.-Y. Liou and Y.-S. Sun, *Macromolecules*, 2012, **45**, 1963–1971.
- G. Renaud, R. Lazzari and F. Leroy, *Surf. Sci. Rep.*, 2009, **64**, 255–380.
- P. Müller-Muschbaum, in *Polymer Surfaces and Interfaces: Characterization and Applications*, ed. M. Stamm, Springer, Berlin, 2008, pp. 17–46.
- R. Lazzari, *J. Appl. Crystallogr.*, 2002, **35**, 406–421.
- J. N. Israelachvili, *Intermolecular & Surface Forces*, Academic Press Inc., 3rd edn, 2011, ch. 17, pp. 415–456.
- R. J. Klein, D. A. Fischer and J. L. Lenhart, *Langmuir*, 2008, **24**, 8187–8197.
- M. M. Browne, G. V. Lubarsky, M. R. Davidson and R. H. Bradley, *Surf. Sci.*, 2004, **553**, 155–167.
- D. O. H. Teare, N. Emmison, C. Ton-That and R. H. Bradley, *Langmuir*, 2000, **16**, 2818–2824.
- C. Ton-That, D. O. H. Teare, P. A. Cambell and R. H. Bradley, *Surf. Sci.*, 1999, **433–435**, 278–282.
- K. Stańczyk, R. Dziembaj, Z. Piwowarska and S. Witkowski, *Carbon*, 1995, **33**, 1383–1392.
- J. R. Pels, F. Kapteijn, J. A. Moulijn, Q. Zhu and K. M. Thomas, *Carbon*, 1995, **33**, 1641–1653.
- A. Elmaci and J. Hacaloglu, *Polym. Degrad. Stab.*, 2009, **94**, 738–743.
- Y. Gao, A. M. Baca, B. Wang and P. R. Ogilby, *Macromolecules*, 1994, **27**, 7041–7048.
- C. Y. Chang, Y. C. Lee, P. J. Wu, J. Y. Liou, Y. S. Sun and B. T. Ko, *Langmuir*, 2011, **27**, 14545–14553.